Available online at www.sciencedirect.com
ScienceDirect
Mechanics of Materials 39 (2007) 340–356
MECHANICS OF MATERIALS
www.elsevier.com/locate/mechmat

# Identification of elastic–plastic anisotropic parameters using instrumented indentation and inverse analysis

Toshio Nakamura *, Yu Gu

*Department of Mechanical Engineering, State University of New York at Stony Brook, Stony Brook, NY 11794, United States*

Received 11 May 2006; received in revised form 22 May 2006

**Abstract**

Mechanical responses of thin films or coatings often display anisotropic behaviors because of their unique microstructures. However, their small size scales can also make determination of material properties difficult. The present paper introduces a simple yet versatile procedure with advanced data interpretation scheme to identify key anisotropic parameters. This procedure utilizes instrumented indentations and an inverse analysis to extract unknown parameters of elastic–plastic transversely isotropic materials. In particular, it post-processes load–displacement records of depth-sensing indentations to obtain best estimates of Young's moduli and yield stresses along longitudinal and transverse directions, respectively. Major advantages of this method are the minimal specimen preparations and the straightforward testing procedure. To enhance the accuracy, the method utilizes two differently profiled indenter heads, spherical and Berkovich. Prior to actual testing, detailed simulations were performed to verify the method's applicability and robustness. In the experiment, a thermally sprayed NiAl coating which possesses process-induced anisotropic features is considered. The load–displacement records of spherical and Berkovich nano-indentations are post-processed with the proposed inverse analysis scheme. The estimated results predict dissimilar responses along the longitudinal and transverse directions. Separate tests are also conducted with micro-indenter heads under larger loads. They demonstrate lesser anisotropic effects but with more compliant responses. These results are attributed to the unique morphology of thermally sprayed coatings, which inherently exhibit size and anisotropic effects.


*Keywords:* Elastic–plastic transversely isotropic; Inverse analysis; Kalman filter; Thin films; Thermally sprayed coatings; Instrumented nano-indenter; Spherical and Berkovich indenters

## 1. Introduction

Thin films and coatings have been widely used in various applications such as large-scale integrated circuits, electronic packaging, sensors, optical films as well as protective and decorative coatings (e.g., Elshabini-Riad and Barlow, 1976). For effective designing and accurate evaluation of their structural integrity, determinations of their mechanical properties are vital for product development. Fabrication techniques for thin film/coating include physical vapor deposition, chemical

* Corresponding author. Fax: +1 631 6328544.
*E-mail address:* toshio.nakamura@sunysb.edu (T. Nakamura).

0167-6636/$ - see front matter © 2006 Elsevier Ltd. All rights reserved.
doi:10.1016/j.mechmat.2006.06.004

vapor deposition, chemical methods (e.g., electroplating), and thermal spray (e.g., plasma spray, combustion spray). Due to these fabrication processes and resulting microstructures, thin films/coatings often exhibit anisotropic mechanical responses. Crystalline/columnar microstructures observed in vapor deposited materials and lamellar microstructures by solidified splats in thermally sprayed coatings are some good examples. Fig. 1 shows a cross-section of atmospheric-plasma sprayed Ni–5wt.%Al coating containing splat and pore/crack morphology. These geometrical features are predominantly aligned along the transverse/horizontal direction (i.e., perpendicular to spray direction) to induce different responses along the longitudinal and transverse directions. Here the longitudinal is defined as the normal to the coating surface or the spray direction while the transverse refers to the two in-plane directions. Although these anisotropic responses of thin films/coatings have been well known, due to their small scales, there are limited experimental procedures to measure their inelastic responses.

For *isotropic* characterizations of thin materials, several notable experimental procedures have been introduced in recent years. Many of them utilize depth-sensing indentations (Fischer-Cripps, 2000). For Young's modulus and hardness, Oliver and Pharr (1992) and Doerner and Nix (1986) proposed methods based on maximum loads and unloading slopes. Field and Swain (1993) also investigated yield stress and strain hardening characteristics. Suresh and Giannakopoulos (1998) and Giannakopoulos and Suresh (1999) introduced effective procedures to quantify residual stresses and elastic–plastic properties of homogeneous materials. Guidelines and assumptions needed for accurate measurements were also discussed by Cheng and Cheng (1999) and Venkatesh et al. (2000). Nakamura et al. (2000) proposed an inverse analysis procedure and instrumented micro-indentation to estimate properties of graded medium using two differently sized spherical heads. Dao et al. (2001) utilized a forward–reverse method and instrumented sharp indentation to characterize elastic–plastic isotropic properties. Chollacoop et al. (2003) improved this method by employing two different indenters with Berkovich and cone heads. In addition, specialized experimental techniques such as bulge testing, substrate curvature, X-ray diffraction, micro-Raman spectroscopy, and electron diffraction contrast imaging, have been developed to determine mechanical properties of both free-standing films and films bonded to substrates (Vinci and Vlassak, 1996). While most of them did not consider the anisotropy, some have considered such effects (Vlassak and Nix, 1994; Vlassaka et al., 2003; Meng and Eesley, 1995; Wang and Lu, 2002). These, however, investigated only *elastic* properties of anisotropic based on indentations along different orientations. For significantly larger specimens, such as rolled-aluminum alloy sheets, there are several studies which considered elastic–plastic anisotropic properties (e.g., Barlat et al., 1997; Wu et al., 2003).

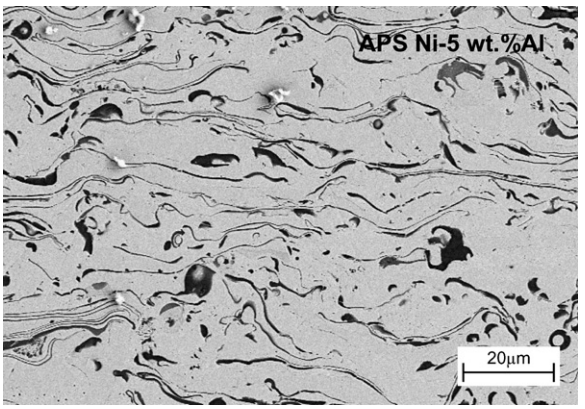


Fig. 1. SEM micrograph showing cross-section of air plasma sprayed Ni–5wt.% Al. The vertical direction corresponds to spray direction (longitudinal). Very dark regions correspond to cracks and pores.

Clearly, a simple examination of load–displacement records from instrumented indentations does not reveal any anisotropic effects. In fact, no explicit correlation between such measurements and anisotropic properties exists. This is the reason an inverse analysis is needed to extract the properties through suitable post-processing of measured records. In general, such processing schemes are necessary when direct relations between measurements and unknown variables are not available or obvious. In the past, various inverse approaches have been utilized in mechanics of material problems. For examples, it was used to detect and quantify critical damage mechanisms like cracking, delamination, and corrosion in aerospace and civil structures (e.g., Chang, 2000). However, an inverse analysis technique is not valuable unless it satisfies convergence and consistency conditions. In many cases, direct implementations of inverse analysis techniques lead to inaccurate solutions due to ill-posed conditions (i.e., non-convergence to unique

solutions). A robust procedure requires suitable technique and proper tailoring. Furthermore, a detailed verification analysis is always necessary *prior* to its application in actual tests. Here, finite element simulations are performed to evaluate its accuracy as well as robustness. The main advantage of proposed method is the simplicity of specimen preparation as well as measurement process. Since indentations are used for the measurement, a free-standing specimen that requires a separation of film/coating from its substrate is not necessary. The separation process can be difficult and often alters the properties of film/coatings.

## 2. Nano-indentation and material models

### 2.1. Dual indentations

In order to obtain as much information on material responses as possible without resorting to a more complex measurement process, two separate indenter heads, Berkovich and spherical are utilized. These differently shaped heads, one is sharp while the other is round, generate different deformation fields (discussed in Section 3.4), and thus offer additional information on material behaviors. The use of dual indenters only adds small testing effort. Note both heads only indent onto a top *free-surface* of specimen. Recently, some attempts were made to indent onto a side *lateral* surface to quantify the anisotropy (e.g., Sampath et al., 2004). However the lateral indentation introduces two complexities. First, indentations on (thinner) lateral planes of thin films are usually difficult because of small scale. In fact, to avoid boundary effects, the specimen must be sufficiently thick, which excludes very thin films ($t < \sim 5$ μm) from testing. Second, correct interpretations of material response requires full 3D analysis for anisotropic materials which can be costly. Thus, in view of keeping the measurements and post-analysis straightforward, indentations onto transverse planes are not considered here.

In the present test, indentations are carried with a nano-indenter from Micro-Materials, Ltd., whose schematic is shown in Fig. 2. This nano-scale indenter has maximum loading range of 350 mN and depth resolution of 15 nm. The schematics of Berkovich and spherical indentations are illustrated in Fig. 3. The Berkovich indenter has a diamond tip ($E = 1140$ GPa, $\nu = 0.07$) while the spherical indenter has a sapphire tip ($E = 335$ GPa, $\nu = 0.25$) and

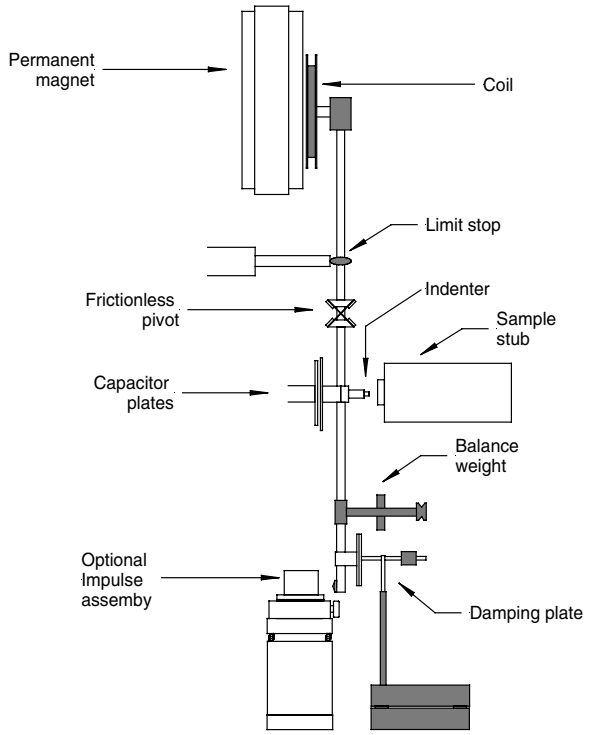


Fig. 2. Schematic of the nano-indentation platform.

the radius of curvature is 270 μm (measured from micrograph). Prior to the test, the machine compliance was determined by calibrated indentations onto a fused quartz sample and the compliance values were adjusted from the load–displacement records. Note that both indenters have much higher modulus and hardness than those of test specimen and they are capable of generating large plastic deformation in the specimen.

### 2.2. Specimens

The test specimen chosen for our analysis was atmospheric-plasma sprayed (APS) Ni–5wt.% Al ($t = 290$ μm) coating. This material is often used as bond coats for thermal barrier coatings on turbine components because of its good adhesion characteristics. The material selection was made based on well known anisotropic characteristics of APS materials. We have also tested EB-PVD copper coating. However it exhibited limited plasticity and was not suitable to evaluate the feasibility of proposed method. Due to inhomogeneous microstructures of thermally sprayed coatings (as shown in Fig. 1), interpretation of indented measurements

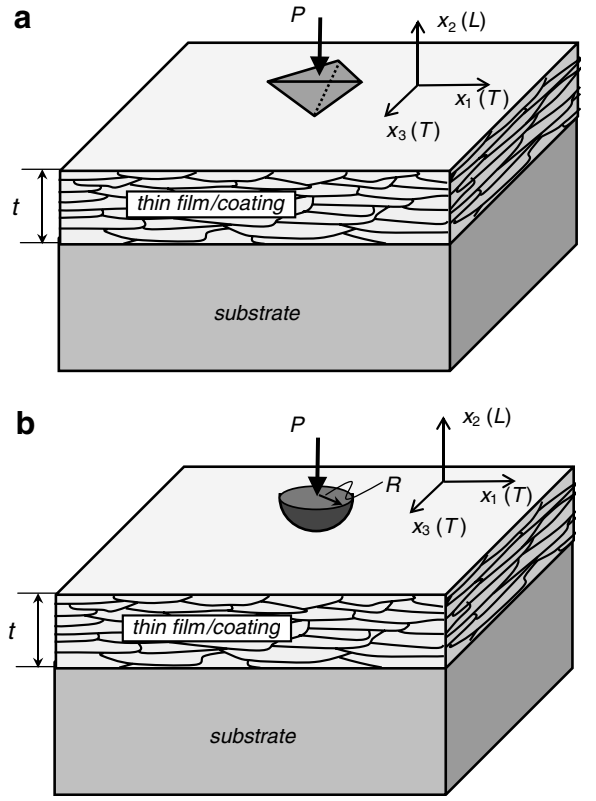


Fig. 3. Schematics of dual indentations, (a) Berkovich and (b) spherical. Anisotropic directions are noted with L (longitudinal) and T (transverse).

requires a special care. Depending upon the indentation location, measured load–displacement record may vary substantially. In fact the morphology underneath the contact (e.g., center of splat or splat–splat interfaces) dictates the deformation characteristics. With NiAl tested here, the displacement variability among different indentations was about ±10% at the constant peak load. Note, the sizes or microstructural inhomogeneity can exceed 10 μm while the indentation depths are less than 1 μm. This means, even with polished surfaces, the irregularities underneath indentation can affect the measurements. Since the purpose of current analysis is to study the feasibility of proposed method, we did not probe into the variability effect in details. Instead, an *average* of load–displacement curves generated from 10 separate indentations was used as the input in the data analysis. Therefore the results reported here should be treated as the averaged properties. Future studies are needed to elucidate this aspect of thermally sprayed materials.

In order to further demonstrate the applicability of proposed method, micro-indentation tests, which have much larger indented foot-prints, are also performed. Since a single indentation covers many splats, the measured variability (about ±3%) among different indentation was less than that of nano-indentations. The indentations by micro-indenters offer additional confirmation of the procedure and also reveal the size effects of thermally sprayed coatings. Due to unique microstructures, APS coatings exhibit different responses at various size scales. The size effects on material responses are described in Section 5.3. These tests should prove the versatility of the proposed method and its applicability to thin films/coating systems possessing transversely isotropic properties.

### 2.3. Elastic–plastic transversely isotropic materials

Many thin films and coatings exhibit isotropic response on one plane and rotational symmetry with respect to one axis (usually along the thickness direction), and often their anisotropic responses are modeled as *transversely isotropic*. In a transversely isotropic material, the elastic properties are described by five independent constants. Suppose the $x_1$–$x_3$ plane is the transverse plane of isotropy (see Fig. 3(a)), the stress–strain relations are represented as

$$\begin{bmatrix} \varepsilon_{11} \\ \varepsilon_{22} \\ \varepsilon_{33} \\ \gamma_{12} \\ \gamma_{23} \\ \gamma_{31} \end{bmatrix} = \begin{bmatrix} 1/E_T & -\nu_{LT}/E_L & -\nu_T/E_T & 0 & 0 & 0 \\ -\nu_{TL}/E_T & 1/E_L & -\nu_{TL}/E_T & 0 & 0 & 0 \\ -\nu_T/E_T & -\nu_{LT}/E_L & 1/E_T & 0 & 0 & 0 \\ 0 & 0 & 0 & 1/G_L & 0 & 0 \\ 0 & 0 & 0 & 0 & 1/G_L & 0 \\ 0 & 0 & 0 & 0 & 0 & 1/G_T \end{bmatrix} \begin{bmatrix} \sigma_{11} \\ \sigma_{22} \\ \sigma_{33} \\ \sigma_{12} \\ \sigma_{23} \\ \sigma_{31} \end{bmatrix}. \tag{1}$$

Here, the subscripts 'L' and 'T' denote for the longitudinal and transverse directions, respectively. The Poisson's ratios $\nu_{LT}$ and $\nu_{TL}$ are related as

$$\frac{\nu_{TL}}{E_T} = \frac{\nu_{LT}}{E_L}. \tag{2}$$

The in-plane ($x_1$–$x_3$ plane) shear modulus can be also expressed as

$$G_T = \frac{E_T}{2(1+\nu_T)}. \tag{3}$$

For the plastic yielding of anisotropic body, Hill's criterion (1948) for orthotropic materials is adopted. His yield function is modified for transversely isotropic materials as

$$f(\sigma)=\sqrt{A(\sigma_{11}-\sigma_{22})^2+A(\sigma_{22}-\sigma_{33})^2+B(\sigma_{33}-\sigma_{11})^2+2C\tau_{12}^2+2C\tau_{23}^2+2D\tau_{31}^2}-\sigma_0=0. \tag{4}$$

Here $\sigma_0$ is the reference stress, and $A \sim D$ are the dimensionless constants related to $\sigma_0$ as

$$A=\frac{1}{2}\left(\frac{\sigma_0}{\sigma_{0L}}\right)^2,\quad B=\frac{1}{2}\left(\frac{2\sigma_0^2}{\sigma_{0T}^2}-\frac{\sigma_0^2}{\sigma_{0L}^2}\right),$$
$$C=\frac{1}{2}\left(\frac{\sigma_0}{\tau_{0L}}\right)^2,\quad D=\frac{1}{2}\left(\frac{\sigma_0}{\tau_{0T}}\right)^2. \tag{5}$$

In the above, $\sigma_{0L}$, $\sigma_{0T}$, $\tau_{0L}$ and $\tau_{0T}$ are the yield stresses along the respective directions. In the current model, the post-yielding behavior was assumed to be represented by a power-law hardening with a constant hardening exponent. In terms of uniaxial stress and strain, the constitutive relations along longitudinal and transverse directions are

$$\varepsilon_L=\frac{\sigma_{0L}}{E_L}\left(\frac{\sigma_L}{\sigma_{0L}}\right)^n \quad \text{for } \sigma_L>\sigma_{0L} \quad \text{and}$$
$$\varepsilon_T=\frac{\sigma_{0T}}{E_T}\left(\frac{\sigma_T}{\sigma_{0T}}\right)^n \quad \text{for } \sigma_T>\sigma_{0T}. \tag{6}$$

where $\varepsilon_L$ and $\varepsilon_T$ are anisotropic strains and $n$ is the strain hardening exponent. For simplicity, the same exponent was assumed for the longitudinal and transverse directions since separate estimations *with reasonable accuracy* would not be possible from indentation measurements. However any difference in actual post-yielding hardening behaviors is implicitly approximated in the estimated values of yield stresses along L and T. In other words, if the exponents are different, the estimated yield stresses are adjusted to offset the error. In summary, the present transversely isotropic material is described by *five* elastic constants, *four* yielding stresses, and *one* hardening exponent.

### 2.4. Unknown material parameters

The present procedure is designed to estimate the material parameters of anisotropic materials. However, it is very difficult and perhaps not practical to determine the entire 10 unknown constants needed to define the elastic–plastic behavior of transversely isotropic materials. Instead we concentrate on extracting key parameters of such materials. They are the Young's moduli and yield stresses along the longitudinal and transverse directions, respectively, and the hardening exponent $n$. In the process to reduce the total number of independent material variables, some assumptions are made *a priori*.

First, all the Poisson's ratios are presumed. Although the measurements of Poisson's ratios of isotropic materials have been carried out with techniques like ultrasound (e.g., Hardwick, 1987; Li et al., 2001; Lasaygues and Pithioux, 2002), it would be difficult to obtain accurate values for anisotropic films/coatings. Here, the Poisson's ratio in the transverse plane $\nu_T$ was assumed as 0.25, which is close to the bulk NiAl system. Second, the sum of two other Poisson's ratios is defined as twice of $\nu_T$, i.e., $\nu_{TL}+\nu_{LT}=2\nu_T$ (note $\nu_{TL}$ and $\nu_{LT}$ are not constant as modulus changes). Third, the out-of-plane shear modulus was approximated as

$$G_L=\frac{(E_T+E_L)/2}{2[1+(\nu_{TL}+\nu_{LT})/2]}. \tag{7}$$

This follows the definition of $G_T$ shown in (3). These approximations should be valid (within a reasonable accuracy) since the differences in properties along the transverse and longitudinal directions of materials considered are not as large as those of fiber-reinforced composites materials (where $E_T$ and $E_L$ are more than a magnitude different). These assumptions reduce the independent elastic parameters to $E_T$ and $E_L$.

For the plastic parameters, shear yield stresses are set according to the von Mises criterion (i.e., $\tau_0=\sigma_0/\sqrt{3}$) as

$$\tau_{0T}=\frac{\sigma_0}{\sqrt{3}} \quad \text{and} \quad \tau_{0L}=\frac{\sigma_0}{\sqrt{3}}\sqrt{\frac{\sigma_{0L}}{\sigma_{0T}}}. \tag{8}$$

Here, the reference stress $\sigma_0$ is defined as the mean tensile yield stress, $\sigma_0=(\sigma_{0T}+\sigma_{0L})/2$. The above equations leave the unknown plastic parameters to be $\sigma_{0T}$, $\sigma_{0L}$ and $n$. Together with the elastic constants, five unknown values are estimated from the proposed procedure.

## 3. Parameter identification procedure

### 3.1. Estimation process

Even with the reduction of unknown parameters, simultaneous estimations of five parameters are not realistic. An optimum approach is to separate the estimation process in steps. First, the mean Young's modulus is defined as $E_m=(E_T+E_L)/2$, and its value is estimated. Due to pile-ups and other physical factors, measured Young's modulus from

indentation often contains a substantial error (even in *isotropic* solids), especially when the material is ductile (Hay and Pharr, 1999; Giannakopoulos and Suresh, 1999). Thus, it makes more sense to estimate the mean modulus and then the modulus ratio ($E_T/E_L$), instead of directly determining individual $E_T$ and $E_L$. The mean modulus is measured using the well-established Oliver and Pharr method (1992) which uses the *unloading portion* of load–displacement curve. Since the present procedure utilizes both spherical and Berkovich indentations, $E_m$ is computed from the average of two measurements. This process should limit a possible error in the estimated ratio $E_T/E_L$ even if a large error exists in the estimated $E_m$. In fact our sensitivity study shows that small change in $E_m$ does not translate to a larger deviation in $E_T/E_L$ (discussed in Section 5.1). Since the determination of $E_m$ is made from the unloading part of indentations and this data is not used to estimate the other parameters, reuse of same data is avoided.

Next, the strain hardening exponent $n$ is estimated from the method introduced by Dao et al. (2001) for *isotropic* elastic–plastic material. As noted by Chollacoop et al. (2003), accurate determination of $n$ is difficult with indentations although the problem can be overcome by multiple indenters. However, for anisotropic materials such an approach is not feasible since it would require development of very complex forward solutions. Furthermore, a small perturbation in $n$ does not significantly alter the *overall stress–strain relation* since any deviation of $n$ is compensated by the estimated value of yield stress $\sigma_0$. Suppose an estimate of $n$ is larger (less hardening) than the actual value, then the estimate of $\sigma_0$ (subsequently made) would be larger than the correct value to offset the error in $n$. This means the actual and estimated stress–strain curves would still look similar except near the yield point. Although the present method utilized the technique developed for isotropic materials with Berkovich indentation (Dao et al., 2001), one may opt to use a bulk material's hardening value for $n$. Either approach should not cause significant error in the estimated stress–strain relation at least within some range of plastic strains. After $E_m$ and $n$ are estimated, the remaining unknown parameters $E_T/E_L$, $\sigma_{0T}$, and $\sigma_{0L}$ are estimated using the inverse analysis described next.

### 3.2. Inverse analysis

In the inverse analysis technique, Kalman filter (Kalman, 1960) is utilized. This technique is widely used in many areas of engineering such as sensor calibration, tracking applications, trajectory determination and signal processing. The Kalman filter algorithm has an advantage over other adaptive algorithms through its fast convergence to optimal solutions in nonlinear problems. Here the algorithm was tailored to estimate three unknown parameters from two measurement records.

In the formulation, the three unknown parameters are represented in a state vector form as $\boldsymbol{x}_t = [(E_T/E_L)_t, (\sigma_{0T}/\sigma_{0L})_t, (\sigma_0)_t]^T$. Here $t$ may represent actual or load step/increment (e.g., from $P_{min}$ to $P_{max}$). The successive estimates for $\boldsymbol{x}_t$ are indirectly made from the indented displacements $\Delta_t^{Berk}$ and $\Delta_t^{Sphe}$, measured with Berkovich and spherical heads, respectively. Since they have different load ranges, actual loading level at a given $t$ is different while the total numbers of increments are kept the same. At $t = 0$, the initial estimates $\boldsymbol{x}_0 = [(E_T/E_L)_0, (\sigma_{0T}/\sigma_{0L})_0, (\sigma_0)_0]^T$ are assigned and the subsequent estimates (at $t = 1, 2, 3, \ldots$) are made according to the following equation:

$$\boldsymbol{x}_t = \boldsymbol{x}_{t-1} + \boldsymbol{K}_t[\boldsymbol{D}_t^{meas} - \boldsymbol{D}_t(\boldsymbol{x}_{t-1})]. \tag{9}$$

Here, $\boldsymbol{K}_t$ is the 'Kalman gain matrix' and $\boldsymbol{D}_t^{meas}$ is a vector containing measured displacements (i.e., $\boldsymbol{D}_t^{meas} = (\Delta_t^{Berk}, \Delta_t^{Sphe})^T$) at $t$. Also $\boldsymbol{D}_t(\boldsymbol{x}_{t-1})$ is a vector containing measured parameters computed with estimated unknown state parameters at the previous increment. Note that these computations require solutions of measured parameters for a given set of state parameters. Such solutions are sometimes referred as the 'forward' solutions. In the above equation, the Kalman gain matrix multiplies the difference between the measured and computed displacements to make corrections to the unknown state parameters. The Kalman gain matrix is computed as

$$\boldsymbol{K}_t = \boldsymbol{P}_t \boldsymbol{d}_t^T \boldsymbol{R}_t^{-1} \quad \text{where}$$
$$\boldsymbol{P}_t = \boldsymbol{P}_{t-1} - \boldsymbol{P}_{t-1}\boldsymbol{d}_t^T(\boldsymbol{d}_t\boldsymbol{P}_{t-1}\boldsymbol{d}_t^T + \boldsymbol{R}_t)^{-1}\boldsymbol{d}_t\boldsymbol{P}_{t-1}. \tag{10}$$

With three state and two measured parameters, the size of Kalman gain matrix is $3 \times 2$. Also $\boldsymbol{d}_t$ is a $2 \times 3$ matrix that contains the gradients of $\boldsymbol{D}_t$ with respect to the state parameters as

$$\boldsymbol{d}_t = \frac{\partial \mathbf{D}_t}{\partial \mathbf{x}_t} = \begin{pmatrix} \dfrac{\partial \Delta_t^{Berk}}{\partial (E_T/E_L)} & \dfrac{\partial \Delta_t^{Berk}}{\partial (\sigma_{0T}/\sigma_{0L})} & \dfrac{\partial \Delta_t^{Berk}}{\partial \sigma_0} \\ \dfrac{\partial \Delta_t^{Sphe}}{\partial (E_T/E_L)} & \dfrac{\partial \Delta_t^{Sphe}}{\partial (\sigma_{0T}/\sigma_{0L})} & \dfrac{\partial \Delta_t^{Sphe}}{\partial \sigma_0} \end{pmatrix}. \tag{11}$$

In addition, $\boldsymbol{P}_t$ is the 'measurement covariance matrix', related to the range of unknown state parameters at increment $t$, and, $\boldsymbol{R}_t$ is the 'error covariance matrix', related to the size of measurement error. Once the initial values are imposed, $\boldsymbol{P}_t$ is updated every step, while $\boldsymbol{R}_t$ is must be prescribed at each step. However, in many cases, fixed values can be assigned to the components of $\boldsymbol{R}_t$ as long as measurement error bounds do not vary substantially during the duration of measurements. Since the convergence rate is sensitive to the values of $\boldsymbol{P}_t$ and $\boldsymbol{R}_t$, proper assignments for these two matrices are essential. The initial measurement covariance matrix $\boldsymbol{P}_0$ and the error covariance matrix $\boldsymbol{R}_t$ are set as

$$\boldsymbol{P}_0 = \begin{pmatrix} (\Delta(E_{\mathrm{T}}/E_{\mathrm{L}}))^2 & 0 & 0 \\ 0 & (\Delta(\sigma_{0\mathrm{T}}/\sigma_{0\mathrm{L}}))^2 & 0 \\ 0 & 0 & (\Delta\sigma_0)^2 \end{pmatrix}$$

$$\text{and} \quad \boldsymbol{R}_t = \begin{pmatrix} (R^{\mathrm{Berk}})^2 & 0 \\ 0 & (R^{\mathrm{Sphe}})^2 \end{pmatrix}. \tag{12}$$

Here $\Delta(E_{\mathrm{T}}/E_{\mathrm{L}}), \Delta(\sigma_{0\mathrm{T}}/\sigma_{0\mathrm{L}})$ and $\Delta\sigma_0$ denote the predicted ranges of the unknown parameters, respectively. While $\boldsymbol{P}_0$ is diagonal, the procedure results in a filled $\boldsymbol{P}_t$ matrix during subsequent increments. In the current analysis, the diagonal components of $\boldsymbol{R}_t$ are chosen based on the estimated measurement error for the weight and the strain measurements. The values of $R^{\mathrm{Berk}}$ and $R^{\mathrm{Sphe}}$ are set approximately 1% of the respective displacements at the maximum loads. The Kalman filter procedure, which is summarized in Fig. 4, is implemented in a computational code.

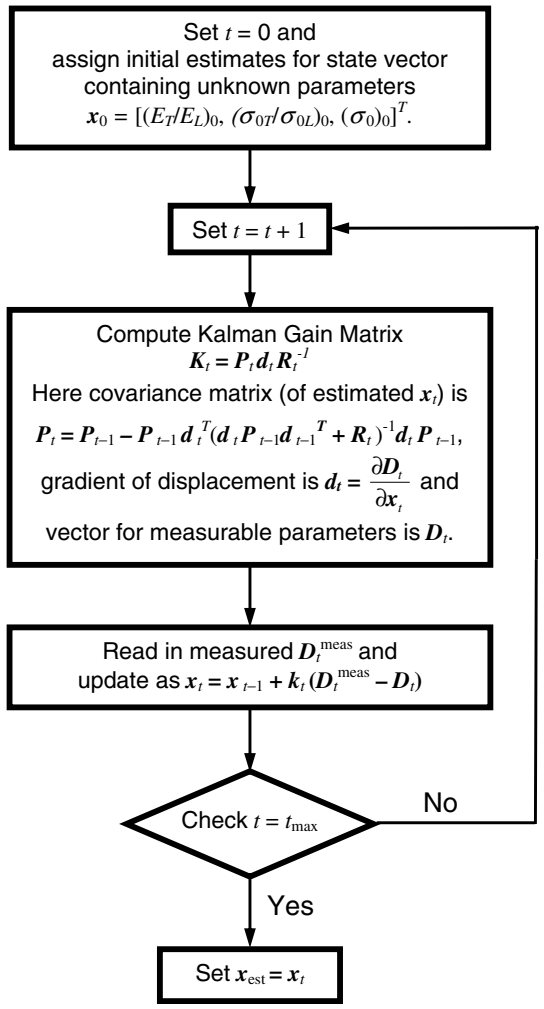


Fig. 4. Flow chart of Kalman filter procedure to determine the unknown parameters using instrumented indentation records.

### 3.3. Reference data via finite element model

Any inverse analyses require at least some knowledge of relations between unknown state parameters and measurable parameters. Here the Kalman filter algorithm requires load-dependent solutions of indented displacements as functions of given state parameters. As no simple solutions, which explicitly account for the anisotropic plastic flow, are available, detailed finite element simulations are carried out to construct the reference data or so-called forward solutions.

The reference data comprise of displacements and their gradients for various values of $E_{\mathrm{T}}/E_{\mathrm{L}}$, $\sigma_{0\mathrm{T}}/\sigma_{0\mathrm{L}}$ and $\sigma_0$ for the load range of interest and they were computed with axisymmetric finite element models. Here a conical model was assumed to represent the Berkovich indenter. This is a commonly used approach to circumvent costly 3D calculations. Here the cone angle is set to 140.6° to represent the same projected area-to-depth ratio as the Berkovich indenter (Fischer-Cripps, 2000). During the mesh construction, careful steps were taken to minimize the instability which can occur near the perimeter of indentation (due to sudden rotation of element surfaces). An enlarged finite element mesh of the coating near the contact region is shown in Fig. 5. The finite element model contains approximately 8200 axisymmetric four-noded elements. A contact condition is prescribed along the boundary between the indenter and coating. For the materials and loading conditions considered here, there were essentially no effects of friction as

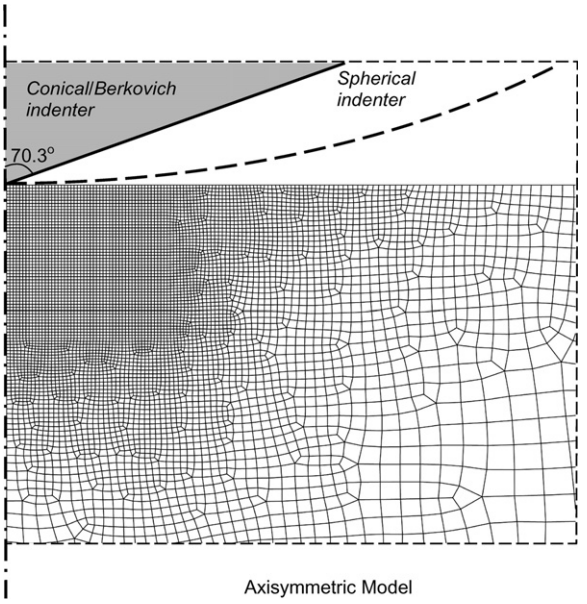


Fig. 5. Local axisymmetric finite element mesh of thin film near indentation. Profiles of conical (approximates Berkovich with cone angle 140.6°) and spherical indenters are shown.

the sliding between the indenter and the surfaces is very limited. Although the actual specimen is attached to a steel substrate, the dimensions of coating are large enough with respect to the indentation sizes to avoid any substrate and outer boundary effects.

### 3.4. Simulated indentation of transversely isotropic materials

Prior to generating reference data, a sample stress–strain relation was used to evaluate indentation responses of a transversely isotropic material. The prescribed uniaxial stress–strain curves along longitudinal and transverse directions of a fictitious material are shown in Fig. 6(a). These material values are arbitrary chosen although they are similar in magnitudes with those of actual specimen. Simulated load–displacement records from the dual indentations are shown in Fig. 6(b) with the unloading portions represented in dashed lines. In the present analysis, the choice of peak or maximum load is vital. Since the elastic–plastic properties are sought, the load must be large enough to cause sufficient plastic deformation underneath the indentations. A few trial simulations were conducted to determine the suitable maximum loads. They are chosen as 100 mN and 350 mN for the Berkovich and spherical indenters, respectively. These loads within the

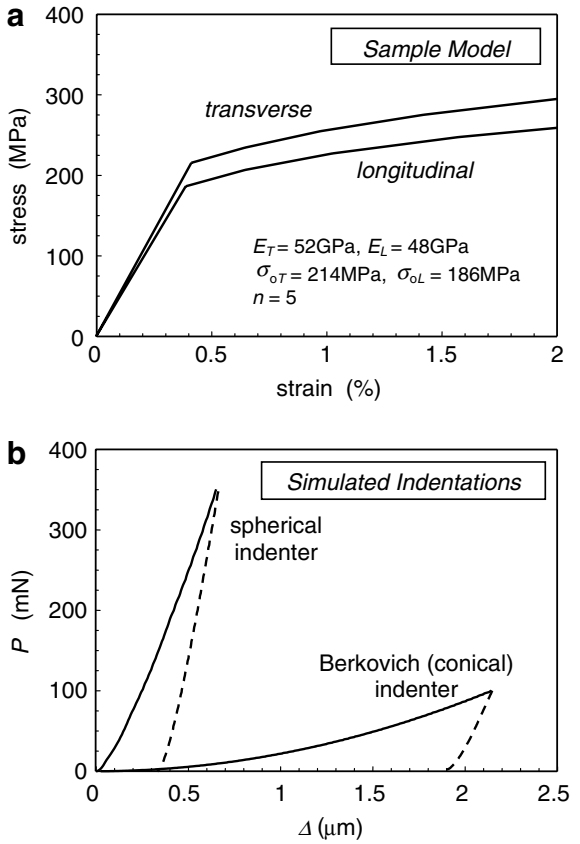


Fig. 6. (a) Uniaxial stress–strain curves along longitudinal and transverse directions of sample transversely isotropic model. (b) Simulated load–displacement indentations curves.

range of optimal load for the present indenter system. Simulations were also performed to evaluate the frictional effects between the heads and specimen surfaces. For the models and materials considered here, basically no effects on load–displacement curves were observed for any frictional coefficients ($0 < \mu_s < 0.9$). Although stress states near the contact were slightly different, the relative energy loss due to friction was minimal.

Some observations can be made from the simulated results. First, substantial differences are displayed in the stress fields under two indentations. The stress contours of $\sigma_z$, $\sigma_r$, $\tau_{rz}$ are shown in Fig. 7 for respective indentations. They clearly exhibit higher stress concentration under the conical (Berkovich) indentation. In contrast, the spherical indentation causes larger spread of high stresses. Its difference with the conical case is most noticeable in the $\sigma_r$ contours. As noted earlier, these *different* characteristics are valuable in obtaining accurate

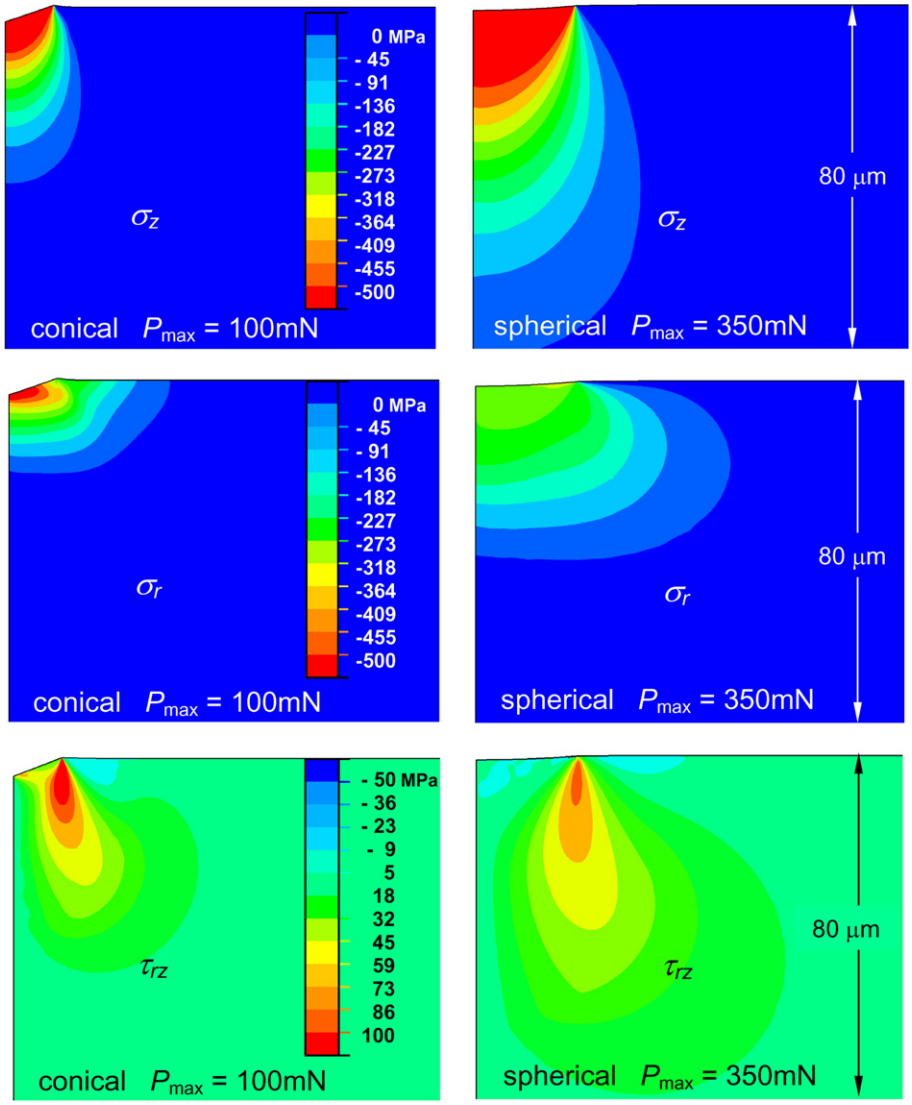


Fig. 7. Axial ($\sigma_z$), radial ($\sigma_r$), and shear ($\tau_{rz}$) stresses near contact region. Conical and spherical indentations display different stress fields.

estimates in the inverse analysis. We also observed the load–displacement curves tend to shift in the opposite direction when the ratio of Young's modulus is changed as illustrated in Fig. 8. With the spherical indentation, *larger* displacements are observed with larger $E_T/E_L$ (for a given load) while *smaller* displacements are observed with the conical indentation. The geometrical shapes of indenters are responsible of these phenomena. The spherical indenter has flatter contact surface and its response is more influenced by the longitudinal modulus $E_L$. On the other hand, the sharper Berkovich indenter gets influenced by the transverse modulus $E_T$ more. These conflicting behaviors exhibited by the two indenters are helpful in estimating the properties since they offer more information to the inverse analysis. In summary, this simulation study supports the utilization of two differently shaped indenters.

### 3.5. Domain of unknown and reference data

The inverse analysis to determine the unknown parameters requires the following steps: (1) set domain/ranges of unknown state parameters; (2) construct reference data; (3) choose optimal load increments for measurement inputs in Kalman Filter process. The domain or bounds of unknowns

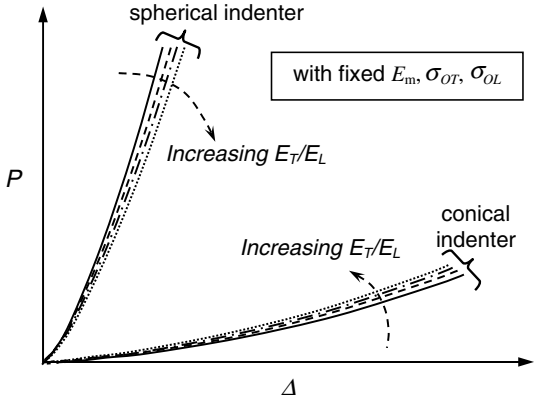


Fig. 8. Schematic of load–displacement curves from conical and spherical indentations. They display opposite behaviors as the modulus ratio changes.

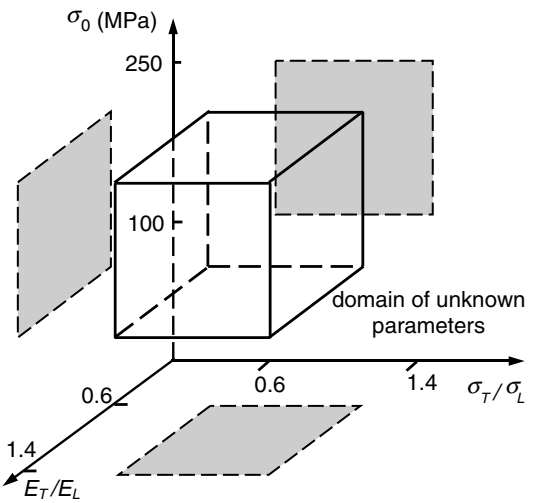


Fig. 9. Domain of three unknown state parameters $E_T/E_L$, $\sigma_{0T}/\sigma_{0L}$, and $\sigma$.

must be chosen carefully since the analysis cannot estimate the unknowns if they fall outside. However, if the convergence is not achieved, the domain size can be always adjusted. In our current studies, known values and earlier studies are used to set the suitable domain size.

For the ratio of elastic moduli in anisotropic materials, there are some experimentally identified results (e.g., Vlassak and Nix, 1994; Meng and Eesley, 1995; Wang and Lu, 2002). They reported that the difference between elastic moduli of different orientations in single crystals can be up to 30%. The transverse modulus $E_T$ of thermal sprayed coating can be significantly higher than longitudinal modulus $E_L$ (Khor et al., 2003). On the other hand, measured anisotropic yield stresses of rolled-aluminum alloy sheets were less than 5% (Barlat et al., 1997; Wu et al., 2003). Based on these references, the domains for $E_T/E_L$ and $\sigma_{0T}/\sigma_{0L}$ are both set from 0.6 to 1.4 in this analysis. These ranges should allow sufficient variations in the transversely isotropic parameters.

For the range of yield stress, $\sigma_0$ was set from 100 MPa to 250 MPa based on previous analysis on sprayed NiAl coatings (Sampath et al., 2004). The domain of three unknown parameters is illustrated in Fig. 9. Using these ranges, the reference data source was constructed. Since many computations with slightly different values of state parameters are not practical, we utilize cubic Lagrangian interpolation functions to compute the load–displacement relations. In this approach, 64 ($=4\times4\times4$) based points are chosen within the domain, and finite element computation is carried out with each set of state parameters. During each calculation, indented displacements at about 100 load steps are recorded. Since both Berkovich and spherical indentation solutions are required, total of 128 separate finite element simulations are carried out. Once these base solutions are made, displacements as well as displacement gradients, for any combinations of state parameters are interpolated at any load level.

## 4. Verification study

Prior to implementing the proposed procedure to estimate unknown properties of real specimens, the inverse analysis was carried out with simulated measurements. Since exact solutions are known in simulations, they can be used to evaluate the accuracy and robustness of the procedure. Because first two steps to estimate the mean modulus and the hardening parameter are already established methods, only the remaining three parameters are estimated here. In the calculation, the material parameters as shown in Fig. 6(a) ($E_T/E_L = 1.08$, $\sigma_{0T}/\sigma_{0L} = 1.16$, $\sigma_0 = 200$ MPa with $E_m = 50$ GPa and $n = 5$) are assumed, and the simulated load–displacement records in Fig. 6(b) are used to backtrack the parameters. For the input, indented displacements at 20 load increments were chosen. For conical/Berkovich indentations, the load range of $P = 20$ mN to 96 mN with intervals of 4 mN, and 40–344 mN with 16 mN intervals for the spherical indentation are chosen.

To obtain unknown parameters with the Kalman filter, initial estimates of $E_T/E_L$, $\sigma_{0T}/\sigma_{0L}$, and $\sigma_0$ must be assigned so that they are updated as the measured parameters are supplied at each load increment. However, final estimates are generally not identical for different initial estimates. In our unique procedure to identify the best estimates, the Kalman filter is carried out with many different initial estimates with their values spread evenly (at $41 \times 41 \times 41 = 68{,}921$ points) in their domain of unknowns shown in Fig. 9. For each set of initial estimates, the Kalman filter computes the final estimates. In order to illustrate the different values of final estimates, a contour plot is constructed. This *intensity of convergence* plot can then be used to identify the most likely values or the *best estimates* of unknowns. A location with large intensity signifies more initial estimates converged near these values of unknowns. A location with high intensity of convergence is chosen for the best estimates. Although three unknowns are estimated simultaneously, their intensity of convergence is shown in three separate 2D plots (for clarity) in Fig. 10. Note that the scale represents a relative intensity and it does not have any physical significance.

In inverse analyses, good convergence characteristics prevail when more measurements are available and unknown state parameters are sensitive to measurement parameters. Furthermore, for a good convergence, the number of measurements is ideally equal to the number of unknowns. Although there are three unknowns with only two measurements (i.e., $P$–$\Delta$ data from dual indentations), a relatively good convergence is obtained because of sufficient sensitivity to the measurements here. Based to the weighted average of converged locations shown in Fig. 10, the best estimates are chosen as $E_T/E_L = 1.06$, $\sigma_{0T}/\sigma_{0L} = 1.18$, $\sigma_0 = 199$ MPa. These values are very close to the exact solutions used to generate the simulated measurements (i.e., $E_T/E_L = 1.08$, $\sigma_{0T}/\sigma_{0L} = 1.16$, $\sigma_0 = 200$ MPa). Thus the verification study supports the effectiveness of proposed approach although the actual implementation still requires additional work as described next.

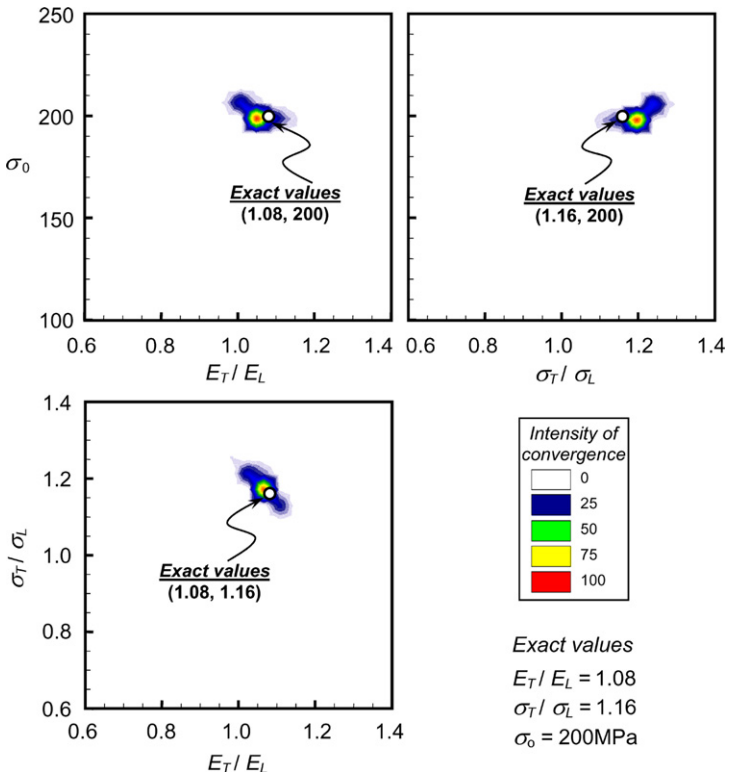


Fig. 10. Intensity of convergence plot generated by the inverse analysis from simulated dual indentation results. A high intensity represents convergence of many initial estimates and likely location of best estimates. The scale of intensity (i.e., 0–100) is relative. The location of exact solutions (i.e., input values) is also noted.

## 5. Anisotropic properties of Ni–5wt.%Al coating

The test specimen, Ni–5wt.%Al coating on steel substrate was fabricated by plasma spray facility at the Center for Thermal Spray Research at SUNY Stony Brook. The feedstock is Metco 4008NS powder with sizes range in 11–45 μm. The substrate temperature was pre-heated at 150 °C. Prior to the indentations, the coating surface was polished using fine emery papers (240, 320 and 600 grit) and diamond suspensions (9, 3 and 1 μm). The final coating thickness was measured as $t = 290$ μm with the dimensions of substrate as 50 mm × 25 mm × 2.5 mm.

### 5.1. Nano-indentation test

First nano-indentations were carried out on the NiAl coating. Similar to the simulation described in Section 4, the maximum load was set at 100 mN for the Berkovich indenter while it was set at 350 mN for the spherical head. For each case, 10 indentations are carried out and the averaged $P$–$\Delta$ curve is determined are shown in Fig. 11. As discussed in Section 2.2, indented displacements at the maximum load exhibited about ±10% variation due to the inhomogeneous morphology of sprayed material. Prior to performing the Kalman filter, the mean values of Young's modulus $E_m$ and the hardening coefficient $n$ are estimated. First the modulus is estimated from the unloading curves of spherical and Berkovich indentations shown in Fig. 11. Using Oliver–Pharr approach (1992) the spherical head predicted 87 GPa and the Berkovich resulted 108 GPa. Here the average of the two is chosen and the mean modulus is set as $E_m = 98$ GPa. As previously noted, this rather large difference is common in indentations of ductile materials. In fact, this is the reason that the modulus ratio instead of individual modulus is chosen as a unknown. The accuracy of $E_m$ estimate will be discussed later. Second, the post-yield hardening parameter was approximated using the forward solutions of Dao et al. (2001). Through an iterative process, the best fit was determined as $n = 2.1$. Again, the preciseness of $n$ is not so critical since any difference is compensated in the subsequent estimate of $\sigma_0$.

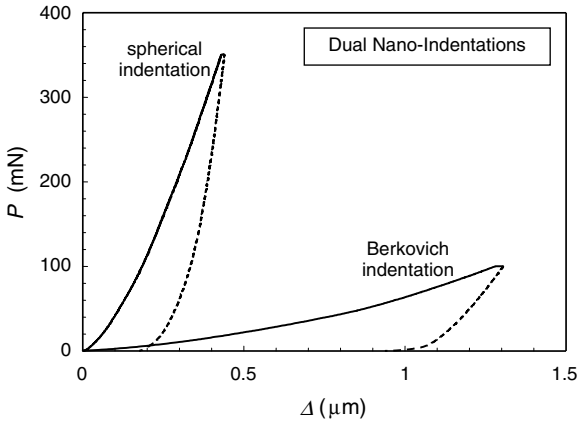


Fig. 11. Measured nano-indentations of plasma sprayed Ni–5wt.%Al coating. Each curve represents average of 10 indentations.

With estimated $E_m$ and $n$, the Kalman filer is carried out using the loading portions of the measured $P$–$\Delta$ records shown in Fig. 11. A similar procedure as described in the verification analysis is followed. The convergence behavior at the final increment is illustrated in the intensity of convergence plots in Fig. 12. At first glance, relatively large domains of convergence (i.e., shaded regions) are observed, especially as compared to the ones shown in Fig. 10 from the numerical simulations. The deterioration is expected since the actual material does not exactly follow the assumed constitutive model and the measurements contain greater errors. However if one concentrates on inspecting regions with higher intensity (e.g., >50), they are sufficiently well-contained. This suggests a reasonable accuracy of the estimates. Based on these plots, the best estimates are identified as $E_T/E_L = 1.07$, $\sigma_{0T}/\sigma_{0L} = 0.77$, and $\sigma_0 = 204$ MPa. The estimates imply slightly stiffer elastic responses along the transverse direction but with lower yielding stress. These results are consistent with preliminary studies on anisotropy of thermally sprayed coatings (e.g., Sampath et al., 2004). Additional measurements are needed to relate the elastic–plastic anisotropic behavior to the microstructures of these materials. Since they are beyond the scope of present study, this aspect will be investigated more closely in a future study. The anisotropic stress–strain curves corresponding to these estimates are shown in Fig. 13(a).

In most inverse analyses, there is no independent way to prove their best estimates are indeed correct or near-correct solutions. However, there are two ways to validate the likeliness of accuracy. One is from the sizes of converged regions shown in the intensity of convergence plots. A small region

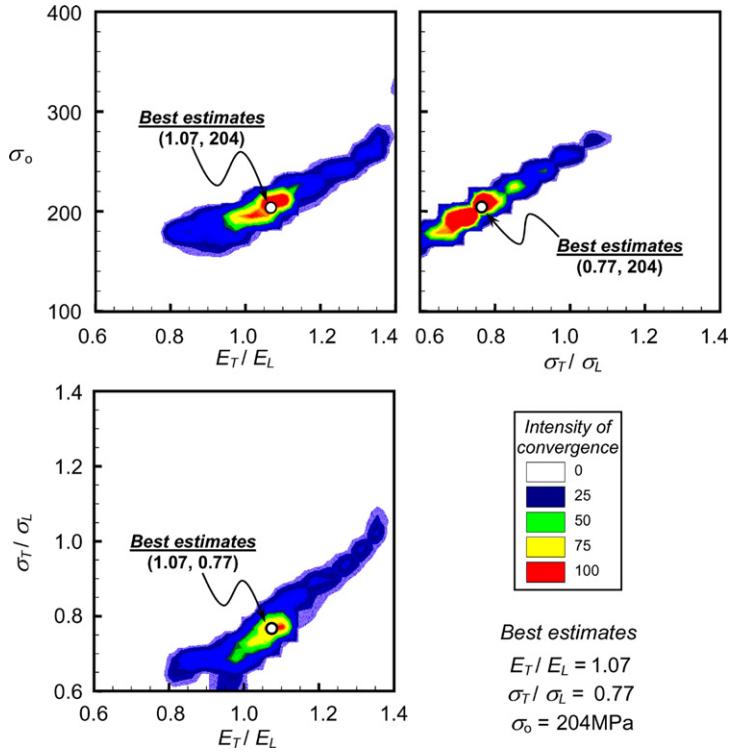


Fig. 12. Intensity of convergence plot generated by the inverse analysis from measured $P$–$\Delta$ records of Berkovich and spherical nano-indentations. The location of best estimates is determined from weighted averages of convergence.

implies that the inverse method is robust since many initial estimates converged near the same location (i.e., similar estimates). The converged regions shown in Fig. 12 are reasonably contained although other analyses (e.g., Gu et al., 2003) have shown better convergences. An additional confirmation on the accuracy can be made from re-simulation of indentation. Using the best estimates identified in the inverse analysis as the inputs, both spherical and Berkovich indentations are simulated again. The computed load–displacement curves are then compared with the actual measurements. As shown in Fig. 13(b), throughout the loading range, the simulated results are close to the measured results (shown with circles).

We have further examined the sensitivity of solutions by assigning slightly different values to $E_T/E_L$ and $\sigma_{0T}/\sigma_{0L}$ (e.g., $E_T/E_L = 1.04$ instead of 1.07), and re-simulated the indentations. Although not shown here, the resulting $P$–$\Delta$ curves consistently exhibited poorer agreements with the measured data than those shown in Fig. 13(b). Although these results still do not prove the uniqueness of solutions, at least they support the likeliness of correct solutions. Furthermore, since small changes in the modulus ratio always produced inferior match with the measurements, the $P$–$\Delta$ curves appear to be sufficiently sensitive to $E_T/E_L$. Essentially it implies (though not proven) that no other values of unknown parameters would produce better fit with the measured data for given material model.

### 5.2. Micro-indentation test

Similar to the nano-scale measurements, dual micro-indentations re also performed to test the applicability of proposed procedure and to probe the size effects of thermally sprayed coatings (see Section 5.3). The tests are conducted with Micro-Material's larger load indenter whose load scale ranges 1–20 N. For the Berkovich test, a standard pyramid diamond tip was used while the spherical indenter is made of carbide-cobalt tungsten whose radius is 795 μm with $E = 614$ GPa and $\nu = 0.22$, respectively. For the micro-indentation, suitable load ranges were also sought prior to actual tests. They were chosen as 3 N and 10 N for the Berkovich and spherical indenters, respectively. The

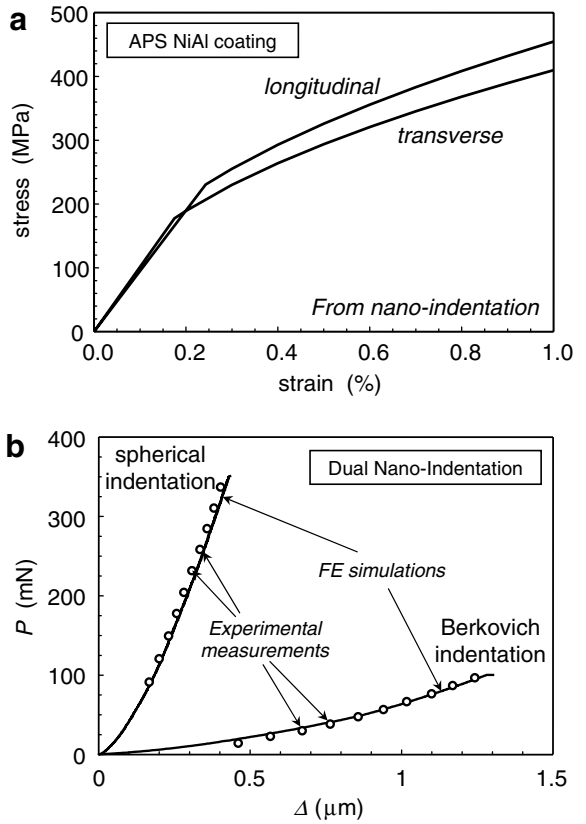


Fig. 13. (a) Transversely isotropic constitutive relation of NiAl coating estimated by the dual nano-indentation and inverse analysis. (b) Comparison between measured and simulated results. The latter solutions are obtained by assigning the best estimates as input properties.

load–displacement measurements are shown in Fig. 14. Prior to performing the Kalman filter, the mean values of Young's modulus $E_m$ and the hardening coefficient $n$ are estimated as well. Using the Oliver–Pharr approach (1992), the spherical case predicted 66 GPa and the Berkovich resulted 70 GPa with the averaged modulus of $E_m = 68$ GPa. The smaller difference obtained here, as compared to that of nano-indentations, is probably due to smaller pile-ups (in relative sizes) with the larger micro-indenters. Again with the forward solutions (Dao et al., 2001), the hardening exponent was estimated as $n = 2.2$, which was close to the one from the nano-test.

For the Kalman filter, 20 load increments are chosen with the load increments ranging $P = 1.0$–2.9 N at equal intervals of 0.1 N for the Berkovich indentation. For the spherical indentation, it is set $P = 2.0$–9.6 N with 0.4 N equal intervals. As in the case of nano-indentations, the domain of unknown

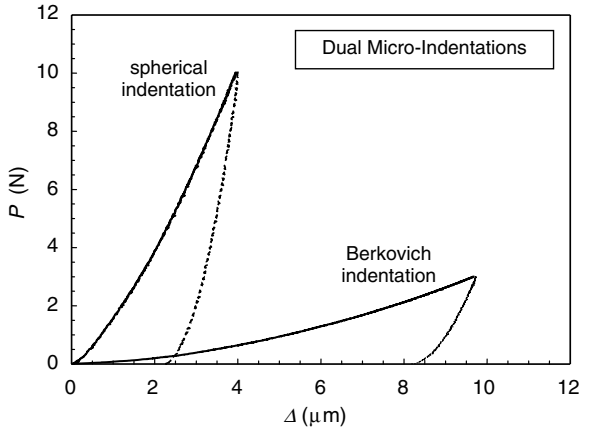


Fig. 14. Measured micro-indentations of air plasma sprayed Ni–5wt.%Al coatings. Each curve represents average of 10 indentations.

parameters as well as corresponding reference data or forward solutions are constructed with separate finite element simulations. The range of mean yield stress is lowered while the ranges for the ratios are kept the same with those of the nano-indentations. The resulting intensity of convergence from the Kalman filter is shown in Fig. 15. The sizes of converged areas are similar to those of nano-indentations which imply a reasonable convergence. Following the same procedure, the best estimates are identified as $E_T/E_L = 1.31$, $\sigma_{0T}/\sigma_{0L} = 0.82$, and $\sigma_0 = 98$ MPa, respectively. Using these parameters, the stress–strain relations based on micro-indentations are constructed as shown in Fig. 16. Although not shown here, simulated $P$–$\Delta$ results with the estimated parameters showed similar agreements with the measured data as those shown for the nano-indentations in Fig. 13(b).

### 5.3. Summary of results

The estimated parameters from both indentations are listed in Table 1. The combined anisotropic stress–strain relations from nano- and micro-measurements shown in Fig. 16 clearly exhibit the size-scale effect. This result is consistent with the well-known mechanical responses of thermally sprayed coatings. With the nano-indenters, the size of region (underneath the indenters) which influences the responses is less than single splat size. Since a splat itself contains limited defects, the its response is stiffener and closer to that of bulk material. For the micro-indentation, more compliant response is obtained since the influencing region is much larger

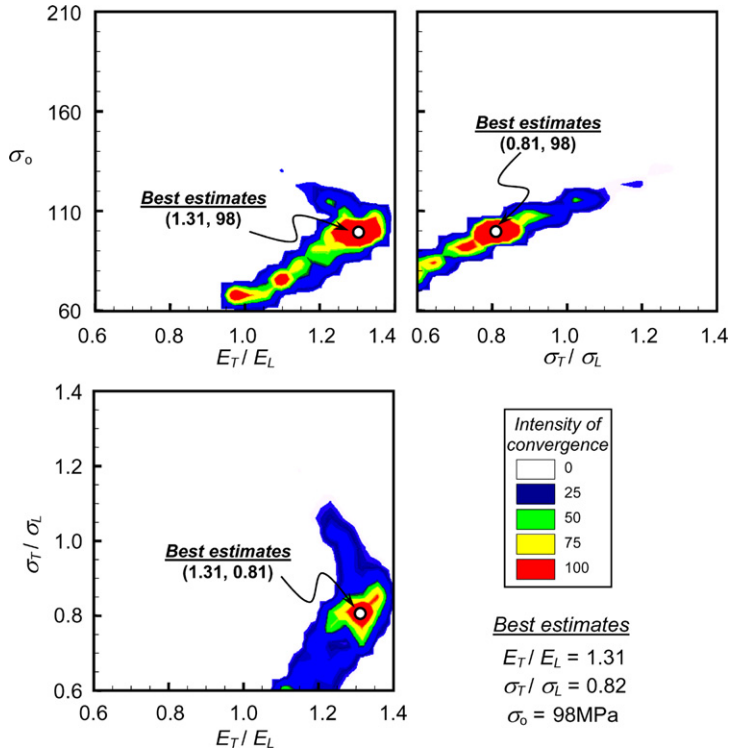


Fig. 15. Intensity of convergence plot generated by the inverse analysis from measured $P$–$\Delta$ records of Berkovich and spherical micro-indentations. The location of best estimates is determined from weighted averages of convergence.

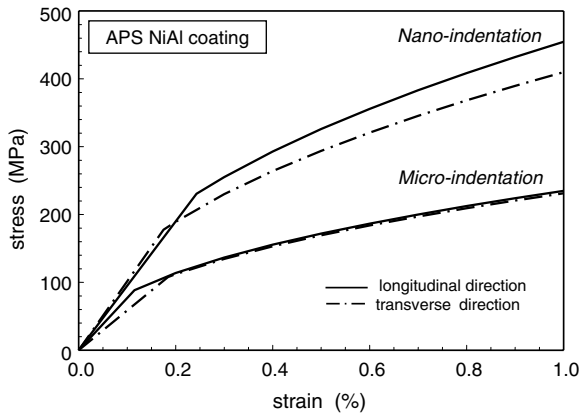


Fig. 16. Transversely isotropic constitutive relation of NiAl coating estimated by nano- and micro-indentations. The difference in responses is attributed to size effect exhibited by plasma sprayed coating.

which encompasses many splats and defects. Also many pores and cracks exist along splat boundaries which make the response to be more compliant.

Detailed investigations of mechanisms causing to the elastic–plastic anisotropic behaviors in plasma-sprayed coatings require additional studies and they are beyond the scope of current study. However, some explanations can be made. The nano-indentation estimates higher yield stress along the longitudinal or spray direction. Due to predominant solidification and cooling along the spray direction, columnar microstructures are often observed within splats. Such geometrical feature may explain the higher yield stress along the longitudinal direction. In the micro-indentations, splat interfaces and cracks/pores also define the indentation responses. Since they are mostly aligned perpendicular to the

Table 1
Estimated anisotropic material properties obtained from instrumented indentations with the inverse analysis

| Ni–5wt.%Al | $E_T$ (GPa) | $E_L$ (GPa) | $\sigma_T$ (MPa) | $\sigma_L$ (MPa) | $n$ |
|---|---|---|---|---|---|
| Nano-indentation | $101 \pm 11$ | $95 \pm 10$ | $177 \pm 21$ | $231 \pm 25$ | $2.1 \pm 0.3$ |
| Micro-indentation | $77 \pm 6$ | $59 \pm 5$ | $88 \pm 8$ | $108 \pm 9$ | $2.2 \pm 0.3$ |

spray direction (longitudinal), the elastic modulus along the transverse direction is greater as observed in Fig. 16. However, in the micro-indentation, the anisotropic effect appears to decrease for higher stresses (i.e., similar strains for a given stress) and also slightly less anisotropy in yield stresses. These phenomena may be caused by larger or more averaged materials are included in its response. Again the physical significance of this behavior is not clear at this point.

## 6. Discussions

In the present study, a novel method to estimate the elastic–plastic anisotropic parameters of thin materials is proposed and examined. The main goal is to establish a method which requires minimal specimen preparation as well as testing effort. Our verification study as well as its initial applications to actual thermally sprayed NiAl coatings demonstrated promising results. The method relies on two common types of indenters, Berkovich and spherical, to gain sufficient information to extract best estimates of unknown properties of transversely isotropic material. Here the five constants are chosen as two Young's moduli $E_L$ and $E_T$, two yield stresses $\sigma_{0L}$ and $\sigma_{0T}$, and post-yielding hardening exponent $n$. First the procedure estimates the mean modulus $E_m$ and the exponent $n$ using the well-established methods for isotropic materials (e.g., Oliver and Pharr, 1992; Dao et al., 2001). Then the remaining three parameters are simultaneously estimated by the Kalman filter technique.

This technique extracts best estimates of unknowns. In the present study, estimated values appeared to be reasonably accurate although an independent confirmation was not made due to lack of available materials with well-known elastic–plastic anisotropic properties. Other approaches to measure elastic–plastic anisotropic properties (even qualitatively) of thin films and coatings are at best limited. In fact, this was the motivation for the present study. Note that there are some MEMS based methods to conduct tensile test of thin specimens. However they are extremely complex and expensive. Furthermore, anisotropic property measurements (including out-of-plane direction) of thin films would be nearly impossible with free-standing specimens. These difficulties suggest the only *viable* measurement to be the one from *instrumented indentations*.

It is important to note that many indentation measurements and their interpreted data contain innate errors due to pile-ups and other physical phenomena associated with their deformation process. The present procedure does not remove these potential errors arising from the indentation process. In reality, this may make the accuracies of estimated anisotropic parameters less than desirable. Nonetheless, the present method can still offer valuable insights to anisotropic characteristics of thin films and coatings, which are very difficult to obtain otherwise. Furthermore, our sensitivity analysis suggests that the estimated *ratios* of modulus and yield stress are not magnified by the potential errors. In fact, it is likely that the errors in estimated ratios are smaller than maximum variations possible with the error bounds noted in Table 1 for the modulus and the yield stress. In other words, though not confirmed, the estimated ratios $E_T/E_L$ and $\sigma_{0T}/\sigma_{0L}$ are more accurate that the individual values.

## Acknowledgements

The authors gratefully acknowledge the supports of the US Army Research Office under the grants DAAD19-02-1-0333, DAAD19-01-1-0709 (equipment) and the National Science Foundation MRSEC program at the SUNY at Stony Brook under the grant # DMR-0080021. We also appreciate S. Singh, G. Bancke and L. Li at Stony Brook for providing nano-indentation and SEM micrograph of NiAl coating. The finite element computations were carried out using the code ABAQUS, which was made available under academic license.

## References

Barlat, F., Maeda, K., Chung, M., Yanagawa, M., Brem, J.C., Hayashie, Y., Lege, D.J., Matsui, K., Murtha, S.J., Hattori, S., Becher, R.C., Makosey, S., 1997. Yield function development for aluminum alloy sheets. Journal of the Mechanics and Physics of Solids 45, 1727–1763.

Chang, F.-K., 2000. Structural Health Monitoring: The Demands and Challenges. CRC Press LLC, Florida.

Cheng, Y.T., Cheng, C.M., 1999. Can stress–strain relationships be obtained from indentation curves using conical and pyramidal indenters. Journal of Materials Research 14 (9), 3493–3496.

Chollacoop, N., Dao, M., Suresh, S., 2003. Depth-sensing instrumented indentation with dual sharp indenters. Acta Materialia 51, 3713–3729.

Dao, M., Chollacoop, N., Vliet, K.J., Van Venkatesh, T.A., Suresh, S., 2001. Computational modeling of the forward and reverse problems in instrumented sharp indentation. Acta Materialia 49, 3899–3918.

Doerner, M.F., Nix, W.D., 1986. A method for interpreting the data from depth-sensing indentation instruments. Journal of Materials Research 1 (4), 601–609.

Elshabini-Riad, A., Barlow, F.D., 1976. Thin Film Technology Handbook. McGraw-Hill Inc., New York.

Field, J.S., Swain, M.V., 1993. A simple predictive model for spherical indentation. Journal of Materials Research 8 (2), 297–306.

Fischer-Cripps, A.C., 2000. A review of analysis methods for sub-micro indentation testing. Vacuum 58, 569–585.

Giannakopoulos, A.E., Suresh, S., 1999. Determination of elastoplastic properties by instrumented sharp indentation. Scripta Materialia 40 (10), 1191–1198.

Gu, Y., Nakamura, T., Prchlik, L., Sampath, S., Wallace, J., 2003. Inverse method to characterize functionally graded material based on experimental records. ELSEVIER Materials Science and Engineering A 345, 223–233.

Hardwick, D.A., 1987. Mechanical properties of thin films: a review. Thin Solid Films 154, 109–124.

Hay, J.C., Pharr, G.M., 1999. A critical examination of the fundamental relations used in the analysis of nanoindentation data. Journal of Material Research 14 (6), 2296–2305.

Hill, R., 1948. A theory of the yielding and plastic flow of anisotropic materials. Proceedings of The Royal Society of London A193, 189–297.

Kalman, R.E., 1960. A new approach to linear filtering and prediction problems. ASME Journal of Basic Engineering 82D, 35–45.

Khor, K.A., Gu, Y.W., Quek, C.H., Chang, P., 2003. Plasma spraying functionally graded hydroxyapatite/Ti–6Al–4V coatings. Surface and Coatings Technology 168, 195–201.

Lasaygues, P., Pithioux, M., 2002. Ultrasonic characterization of orthotropic elastic bovine bones. Ultrasonics 39 (8), 567–573.

Li, Z.-Q., Zhang, X.-R., Zhang, S.-Y., Shen, Z.-H., 2001. Determination of the elastic constants of metal-matrix composites by a laser ultrasound technique. Composites Science and Technology 61 (10), 1457–1463.

Meng, W.J., Eesley, G.L., 1995. Growth and mechanical anisotropy of TiN thin films. Thin Solid Films 271, 108–116.

Nakamura, T., Wang, T., Sampath, S., 2000. Determination of properties of graded materials by inverse analysis and instrumented indentation. Acta Materialia 48, 4293–4306.

Oliver, W.C., Pharr, G.M., 1992. Improved technique for determining hardness and elastic modulus using load and displacement sensing indentation experiments. Journal of Materials Research 7 (6), 1564–1580.

Sampath, S., Jiang, X.Y., Matejicek, J., Prchlik, L., Kulkarni, A., Vaidya, A., 2004. Role of thermal spray processing method on the microstructure, residual stress and properties of coatings: an integrated study for Ni–5Wt.%Al bond coats. Materials Science & Engineering A 364, 216–231.

Suresh, S., Giannakopoulos, A.E., 1998. A new method for estimating residual stresses by instrumented sharp indentation. Acta Materialia 46 (16), 5755–5767.

Venkatesh, T.A., Van Vliet, K.J., Giannakopoulos, A.E., Suresh, S., 2000. Determination of elasto-plastic properties by instrumented sharp indentation: guidelines for property extraction. Scripta Materialia 42 (9), 833–839.

Vinci, R.P., Vlassak, J.J., 1996. Mechanical behavior of thin films. Annual Review of Materials Science 26, 431–462.

Vlassaka, J.J., Ciavarellab, M., Barberc, J.R., Wanga, X., 2003. The indentation modulus of elastically anisotropic materials for indenters of arbitrary shape. Journal of the Mechanics and Physics of Solids 51, 1701–1721.

Vlassak, J.J., Nix, W.D., 1994. Measuring the elastic properties of anisotropic materials by means of indentation experiments. Journal of the Mechanics and Physics of Solids 42 (8), 1223–1245.

Wang, W., Lu, K., 2002. Nanoindentation measurement of hardness and modulus anisotropy in $Ni_3Al$ single crystals. Journal of Materials Research 17 (9), 2314–2320.

Wu, P.D., Jain, M., Savoie, J., MacEwen, S.R., Tugcu, P., Neale, K.W., 2003. Evaluation of anisotropic yield functions for aluminum sheets. International Journal of Plasticity 19, 121–138.